Antenna Integrated THz Uni-Traveling Carrier Photodiodes

Cyril C. Renaud, *Senior Member, IEEE*, Michele Natrella, Chris Graham, James Seddon, Frederic Van Dijk, and Alwyn J. Seeds, *Fellow, IEEE*

(Invited Paper)

***Abstract*—High-speed photodiodes are a key element of numerous photonic systems. With the development of potential applications in the THz range such as sensing, spectroscopy, and wireless transmission, devices with integrated antenna covering the frequency range from 0.1 to 3 THz will become essential. In this paper, we discuss the development of uni-traveling carrier photodiodes with integrated antennas to address that need. In particular we develop the key elements to present a simple design tool for the efficient integration of the device with an antenna. We also present fabricated device results that show the highest figure of merit to date for photonic THz emitters. When integrated with well-matched antennas the devices have achieved record level of power up to 1 THz compared to other published photomixers. We also show that these devices can be used as receivers at frequencies up to 560 GHz with conversion losses of the order of 30 dB.**

***Index Terms*—THz photomixers, THz antennas, UTC-photodiodes, terahertz radiation.**

I. Introduction

RECENT work on high-speed photodetectors has shown significant improvements including higher responsivity [1] through better optical coupling, higher output power [2] and larger bandwidth [3]. These different developments have been key for such devices to find application in a set of photonic systems with ever increasing technical demands. One particular frequency range where photonic solutions have been at the forefront of developments is the millimetre wave to THz range (0.1 THz–10 THz) [4]. In that range, applications such as radar, sensing and broadband wireless communication require solutions that are both frequency agile and offer large bandwidth, which photonics is well placed to provide [4]. To meet these applications requirements, the development of photomixers that are efficient and operate at room temperature [4]–[6] is essential. In this regard two main solutions have emerged; photoconductive antennas and photodiodes. In terms of efficiency, as emitters in the THz range, photodiodes have so far offered the best performances, in particular the uni-travelling carrier photodiode (UTC-PD) [7]–[9] which is a high speed and high output power photodiode [10]–[17]. The response of the UTC-PD is determined by the electron transport in the whole structure. This is an essential difference from the conventional pin PD, where both electrons and holes contribute to the device response, and the low-velocity hole-transport limits the performance. In UTCs electrons exhibit velocity overshoot (3-5 $\times$ 10^7 cm/s) in the carrier collection layer [7]; in addition, the UTC-PD generates higher output saturation current due to the reduced space charge effect in the depletion layer, which also results from the high electron velocity in the depletion layer [9]. Since its invention in 1997 [7], modified UTC-like structures with a hybrid absorber have been developed, to optimise the bandwidth and responsivity [9]. All of the structures consist of narrow-gap absorbers sandwiched by wide-gap p- and n-contact layers. Growth of phosphorus based UTC structures has also been demonstrated by Solid Source Molecular Beam Epitaxy [18]. Particular examples of work to enhance the performances of UTC-PDs include combining a UTC-PD with travelling wave (TW) design [17] and optimisation of the structure to further the point of space charge saturation in modified UTC (MUTC) [2].

One key aspect of developing such devices as emitters or potentially as receivers is to design and optimise fully the integration of the device with a planar antenna. Only through optimised coupling will it be possible to access the full potential of the devices. In this paper, we will discuss the key elements in designing such antenna systems and the methods used in fabrication. We will then show the results obtained from integrated antenna devices both as emitters and receivers showing their outstanding performance, particularly in terms of efficiency in converting optical power to electrical power, where their figure of merit (P_{THz}/P_{opt}^2) is the highest published to date. These results demonstrate clearly the advantages of the overall waveguide design for developing efficient photomixers for THz applications, although there is still scope for work on the optimisation of both optical coupling and antenna design to enhance the efficiency of the emitter further.

Manuscript received May 31, 2017; revised July 4, 2017; accepted July 5, 2017. This work was supported by the Engineering and Physical Sciences Research Council through the COTS Programme under Grant EP/J017671/1, and in part by the European Commission Seventh Framework Programme (FP7-ICT) through IPHOBAC-NG (619870) and PARADIGM (257210) projects. *(Corresponding author: Cyril C. Renaud.)*

C. C. Renaud, M. Natrella, C. Graham, J. Seddon, and A. J. Seeds are with the Department of Electronic and Electrical Engineering, University College London, London WC1E 7JE, U.K. (e-mail: c.renaud@ucl.ac.uk; m.natrella@ucl.ac.uk; c.graham@ucl.ac.uk; james.seddon.14@ucl.ac.uk; a.seeds@ucl.ac.uk).

F. Van Dijk is with the III-V Lab Route départementale 128, Palaiseau 91767, France (e-mail: frederic.vandijk@3-5lab.fr).

Color versions of one or more of the figures in this paper are available online at http://ieeexplore.ieee.org.

Digital Object Identifier 10.1109/JSTQE.2017.2725444

II. Device Design and Impedance Matching

Although UTCs integrated with planar resonant and non-resonant antennas have been demonstrated previously [17], [19], this was mostly done using standard bow tie and log periodic antenna designs with relatively little care being taken to match the impedance of the device with the antenna over as large a frequency range as possible. Developing a design tool for fully matching the antenna to the device is essential if optimised broadband operation is to be obtained. If one looks at how millimetre-wave receivers and transmitters were developed, it would appear that they were traditionally machined waveguide-based antennas [20]. Corrugated horns were built up to 300 GHz and dual-mode horns up to 500 GHz [21], [22]. The travelling wave corner-cube antenna [23], [24], which is an open structure compatible with whisker contacted Schottky diodes, was for a long time the only available receiver at frequencies above 1000 GHz and increasingly optimised versions were realised [25]–[28]. Machined antennas for sub-millimetre-wave and THz frequencies are difficult to realise and expensive. Monolithic receivers based on planar antennas are an attractive solution for the millimetre and sub-millimetre-wave region [29]. Microstrip antennas are simple to fabricate, low cost, lighter and low profile and hence ideal candidates for integration with photomixers; besides, the planar structure of microstrip antennas enables easy fabrication of large antenna arrays. However, microstrip antennas suffer from significant ohmic losses at sub-millimetre-wave and THz frequencies and exhibit reduced performance in terms of bandwidth and directivity in comparison with standard waveguide horns. The substrate thickness for microstrip antennas needs to be small, around one hundredth of the wavelength in free space [30]. At sub-millimetre-wave and THz frequencies this specification is hard to meet as substrates are typically electrically thick, resulting in substrate modes which affect the antenna impedance, radiation efficiency and radiation pattern. The use of the substrate dielectric lens, introduced by Rutledge and Muha in 1981 [31], has become a popular solution to limit substrate modes. As mentioned above, the design of planar antennas to be integrated with photodiodes needs careful consideration and can nowadays benefit greatly from the use of full-wave electromagnetic modelling, even for structures electrically very large. Simple analytical approaches can produce misleading results as they can only be carried out for extremely simplified cases, requiring significant assumptions. An example of such an assumption is considering a planar antenna on substrate lens as equivalent to an antenna on a semi-infinite substrate. When a planar antenna on a substrate lens is studied by means of full-wave modelling, it is found that a significant part of the electric field is trapped within the lens by reflections and generates strong standing waves; as already suggested in [32] the substrate lens may perform more as a resonator than as a lens. Another concern about substrate lenses is that the radiation pattern is sensitive to the alignment between antenna chip and lens and the main lobe can tilt and decrease in amplitude as a result of misalignment. Both standing waves and the effect of misalignment are shown in Fig. 1, which displays the amplitude of the electric field at 350 GHz for a bow-tie antenna on a 4 mm silicon lens in a collimating configuration. As a result of the sensitivity to misalignment, substrate lenses are not suitable for integration with arrays since each antenna element of the array would be significantly misaligned with the lens axis, resulting in a very poor radiation pattern. The reflections inside the lens also affects the antenna impedance as shown in Fig. 2.

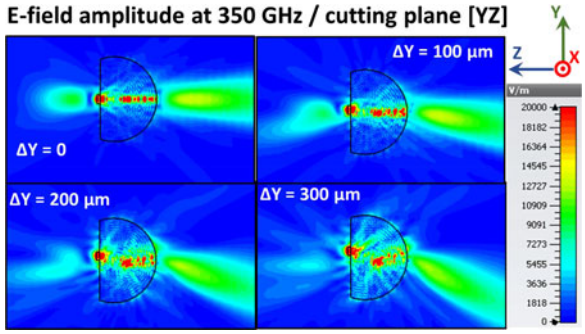

Fig. 1. Cross section views through the lens, showing the electric field amplitude in four cases of increasing misalignment, i.e. $\Delta Y = 0$, $\Delta Y = 100\,\mu$m, $\Delta Y = 200\,\mu$m and $\Delta Y = 300\,\mu$m. Reflections and standing waves inside the lens are visible in all cases.

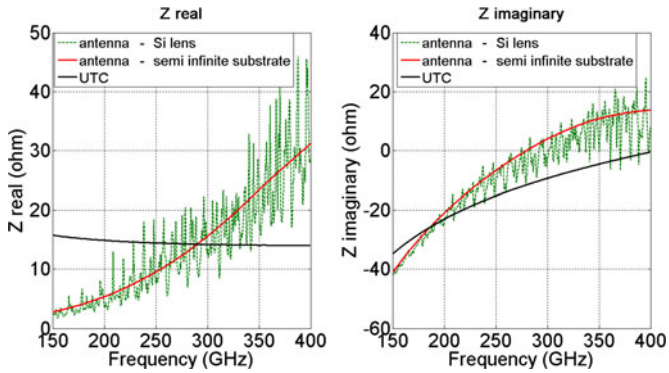

Fig. 2. Comparison between the impedance of a bow-tie antenna integrated with a Si lens (dashed green line) and the impedance of the same antenna on a semi-infinite substrate (solid red line). The impedance of a UTC studied in [30] is also plotted (continuous black line). The antenna is designed to realise complex-conjugate impedance matching with the UTC between 300 and 350 GHz.

Both resistance and reactance of the antenna on the silicon lens oscillate prominently around the ideal values of the antenna on a semi-infinite substrate, with higher frequencies being affected more significantly. Such an erratic coupling efficiency with the source (UTC) could be apparent on a system aiming to generate a tuneable high purity RF signal, generated for instance by heterodyning two phase-locked lasers, since the signal strength would vary significantly even for small (GHz) frequency variations.

In general, design and optimisation of radiation pattern, radiation efficiency and impedance of antennas integrated with photodiodes can greatly benefit from the use of full-wave electromagnetic modelling. Even simple tasks, such as realising the bias connections on the antenna, can result in significant effects on the antenna performance if not carefully modelled.

Research on antenna integrated UTC-PDs is focused on enhancing the emitted power and bandwidth. Emitted power and bandwidth depend on 4 key factors: 1) optical fibre-to-chip coupling efficiency; 2) photodiode bandwidth, optical responsivity

and saturation power; 3) photodiode-to-antenna coupling efficiency; 4) antenna directivity and radiation efficiency. Point 3 (photodiode-to-antenna coupling efficiency) has not received much attention in the literature.

If an antenna is driven by an ideal current source (i.e. having infinite output impedance) then the antenna radiation resistance (i.e. non-lossy part of the impedance real part) should simply be chosen to be as high as possible. The UTC can only be considered as a nearly ideal current source at DC, but has a finite and complex (i.e. not purely resistive) output impedance at higher frequencies. Therefore, to optimise the efficiency of power coupling between UTCs and antennas, complex-conjugate matching needs to be realised. When the source impedance is real, reflection-less matching with the load (antenna) is equivalent to maximum transfer of power matching (i.e. complex-conjugate matching); hence, reducing the reflection coefficient with respect to a resistance equal to the source impedance automatically leads to maximising the transfer of power from the source to the antenna. For these reasons, on the assumption of driving antennas with a real impedance source, the antenna bandwidth in terms of impedance can be defined in terms of reflection coefficient ρ, or S_{11} in dB or VSWR (Voltage Standing Wave Ratio) with typical specifications requiring $\rho < 0.2 \iff S_{11} < -14\,\text{dB} \iff \text{VSWR} < 1.5$.

The broad band concept for antennas should be defined clearly and considered carefully when designing antenna integrated UTCs. Antenna bandwidth has to be defined in terms of both gain (i.e. directivity and radiation efficiency) and efficiency of energy coupling from the source. If an antenna impedance is efficiently matched to its source over a wide frequency range, but its radiation pattern does not maintain a useful profile all across the same frequency range, then such an antenna should not be described as broad band. Antennas like the equiangular spiral and the toothed log- periodic, often integrated with UTCs, have been demonstrated to have constant impedance over a broad frequency range [30], [34], [35]. For this reason they can provide broadband matching to a constant impedance driving source. When these antennas are driven by UTC-PDs, such a broadband matching is harder to achieve since the UTC impedance is not constant, with a strongly frequency dependent reactive component. Hence, the antenna impedance broadband properties need to be considered in conjunction with the complex impedance of the driving source and, for maximisation of the power coupling bandwidth, the impedance of the source should be fully taken into account.

An antenna is defined as resonant at a frequency where its reactance is zero, for instance a frequency corresponding to a wavelength double the antenna length for the case of a classical dipole antenna. Since at such a resonance frequency the antenna impedance is purely resistive, if the source impedance is also purely resistive and equal to the antenna resistance, the coupling efficiency will be very high. The coupling efficiency will decay quite rapidly as the frequency moves away from the resonance. This shows that also in the resonant antenna case, the "resonant antenna" property cannot be fully exploited without taking into account the impedance of the driving source. As a quantitative example, the UTCs characterised experimentally and numerically in [30] exhibited a complex impedance at 100 GHz equal

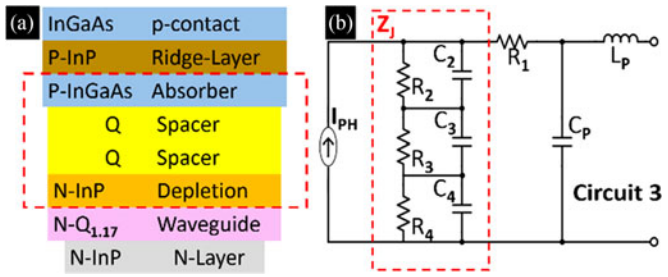

Fig. 3. (a) UTC layer structure. (b) New equivalent circuit, showing the relation with the UTC structure. The two spacers have been modelled as two *RC* parallel circuits (R_2C_2 and R_3C_3). The neutral region of the heavily p-doped 120 nm thick absorber only provides a negligible resistive contribution. The R_4C_4 parallel represents the carrier collection layer, while R_1 takes into account the resistive effects of doped materials and ohmic contacts. C_p and L_p account for parasitic capacitance and inductance respectively.

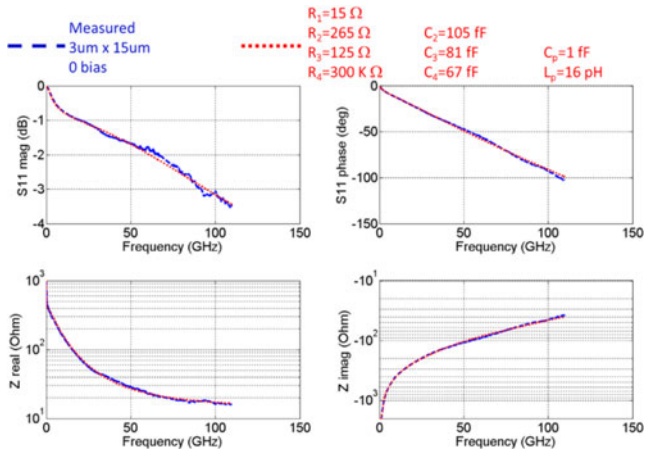

Fig. 4. Comparison between measured S_{11}/impedance of a $3 \times 15\ \mu\text{m}^2$ area UTC at 0 V bias (dashed blue line), and S_{11}/impedance obtained from the circuit which models the proposed effect of spacer layers and conduction band discontinuities (dotted red line).

to $(18 - j57)\,\Omega$. The power coupled from this UTC to an antenna resonant at 100 GHz, with a purely resistive impedance of 18 Ω, would be smaller, by a factor of 5.5 dB, than the power coupled to a non-resonant antenna having an impedance of $(18 + j57)\,\Omega$ also containing an inductive reactance. In [36] it was demonstrated experimentally and numerically that the maxima of power radiated by a bow-tie antenna integrated with a UTC were present where complex-conjugate matching was realised.

Design of optimised antennas for integration with UTCs would therefore greatly benefit from accurate knowledge of the complex UTC source impedance so as to achieve maximum radiated power. In [33] an experimental and semi-analytical study of waveguide UTC impedance up to 110 GHz was presented and a modified circuit model was introduced (Fig. 3), since it was found that the classical diode circuit model [37] cannot fully explain the experimental data, especially in the lower frequency range where parasitic effects are negligible and cannot be used to explain the disagreement.

A mathematical explanation was also presented in [33] to explain why the trend of measured S_{11}/impedance cannot be matched by the standard diode circuit model. As shown in Fig. 4 (UTC grown with gas source MBE –Table I) the modified

TABLE I
EPITAXIAL STRUCTURED USED IN THIS WORK, [17] MOVPE, [18] SOLID SOURCE MBE, [44] GAS SOURCE MBE

TW-UTC-PD [17]				Solid Source MBE UTC-PD [18]				Integrated UTC-PD [44]			
Doping (cm^3)	Material	Function	Thick (nm)	Doping (cm^{-3})	Material	Function	Thick (nm)	Doping (cm^{-3})	Material	Function	Thick (nm)
$>2.10^{18}$	$P^+ Q_{l.3}$	p-contact	200	$>1.10^{19}$	$P^{++} Q_{l.3}$	p-contact	200	P^{++}	GaInAs	p-contact	200
$1.5.10^{18}$	P^+ InGaAs	absorber	120	$2.5.10^{18}$	P^+ InGaAs	absorber	20	P^+	InP	Ridge layer	1000
u.i.d·	n $Q_{1.3}$	spacer	30	1.10^{18}	P^+ InGaAs	absorber	30	P gradual	InGaAs	absorber	120
u.i.d.	n InP	collection	300	5.10^{17}	p InGaAs	absorber	30	n	Q	spacer	–
2.10^{18}	n^+ $Q_{1.3}$	Waveguide	300	$2.5.10^{17}$	P InGaAs	absorber	30	n	Q	spacer	–
4.10^{18}	n InP	n contact	600	u.i.d.	u InGaAS	absorber	10	n	InP	collection	300
–	u $Q_{l.2}$	Diluted wg	40	u.i.d.	u $Q_{1.3}$	spacer	10	n^+	$Q_{l.17}$	Waveguide	300
...	...	...	...	u.i.d.	u$Q_{1.1}$	spacer	10	n^+	InP	n contact	600
Fe	SI InP	substrate	–	1.10^{16}	n InP	Collection	300	Fe	SI InP	Substrate	–
				$2.5.10^{18}$	n^+ $Q_{1.3}$	Waveguide	300				
				$>1.10^{19}$	n^{++} InP S	n contact	700				
				Fe	SI InP	Substrat	–				

circuit can provide excellent agreement with measurements and, as discussed in [33], the same excellent agreement was achieved for devices of different sizes and under different bias. It is essential to note that the S_{11} is a complex quantity therefore, a model can only be claimed to be accurate if calculated modulus and phase simultaneously match measured modulus and phase over the whole frequency range of interest. In [33] it was shown that some set of values of the classical diode circuit parameters, can provide good agreement with the measured S_{11} modulus but fail to match the measured S_{11} phase (or equivalently real and imaginary part of the impedance). An original approach was shown in [38] employing a maximum likelihood estimation procedure for the parameters of the classical diode circuit model. However, regardless of the procedure employed for estimation of the parameters, it needs to be demonstrated that the chosen circuit model can accurately match measured S_{11} modulus and phase simultaneously over the frequency range; in [38] the comparison between calculated and measured S_{11} phase is not shown and the comparison with the modulus is shown only up to relatively low frequencies (15 GHz). If the standard diode circuit model could provide accurate matching to the measured S_{11} over the whole frequency range and fitting its parameters was the scientific problem to solve, then a plethora of commercial software could be used to fit the parameters, without the need to resort to complicated statistical procedures.

The physical meaning of the additional elements in the modified circuit of Fig. 3 has been explained in detail in [33] and associated with the presence of conduction band discontinuities, between the narrow bandgap $In_{0.53}Ga_{0.47}$ As material and large bandgap InP material, affecting the UTC impedance in the lower frequency range. The issue concerning the presence of an offset in the conduction band edge was identified for Heterostructure Bipolar Transistors (HBT) and has been comprehensively studied and reported in the literature [39]–[43].

The set of optimised parameter values obtained for the modified circuit in Fig. 3 is essentially unique. In fact the value of R_1 has to be equal to the measured series resistance (through I-V measurements [44]); the value of R_4 has to be very large and only has some influence at extremely low frequency; the parasitic capacitance and inductance R_P and L_P only count at very high frequencies and are excluded from the fitting process; the three RC parallel circuit elements left are responsible for three poles in the complex S_{11} function and must simultaneously shape its modulus and phase from near DC to high frequency.

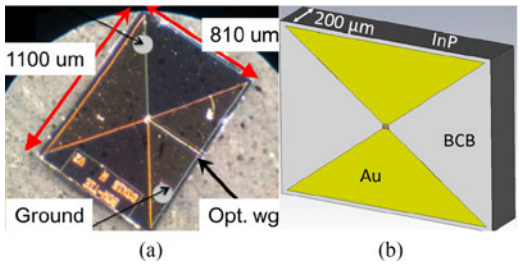

Fig. 5. a) Bow-tie antenna integrated UTC (Gas source MBE in Table I) with a ground plane. The photodetector area is 3×15 μm^2 and the antenna-chip approximate geometrical details are shown in the picture; b) CST model of the bow-tie antenna with a gold ground plane.

Building on this comprehensive study of the UTC impedance, detailed 3D full-wave modelling was later employed [36] to extend the knowledge of UTC impedance and photo-response up to 400 GHz.

The total power emitted by an antenna depends on the impedance match with the driving source and on the radiation efficiency. The former defines the fraction of power made available by the source that is accepted by the antenna, while the latter determines the fraction of power accepted by the antenna that is coupled into free space. The antenna directivity only describes the angular distribution of the radiated power. Therefore the absolute level of power emitted by an antenna over the frequency range can only be calculated and predicted if the source impedance is also known and the coupling efficiency between UTC and antenna taken into account.

In [36] it was demonstrated that the knowledge of the UTC impedance can enable a good prediction of the absolute level of power radiated over the frequency range by an antenna driven by the same UTC. To this end the power emitted by an antenna integrated with one of the UTCs (Gas source MBE UTC–Table I) studied in [33] (Fig. 5) was measured, between 65 GHz and 185 GHz, and compared to the power calculated with

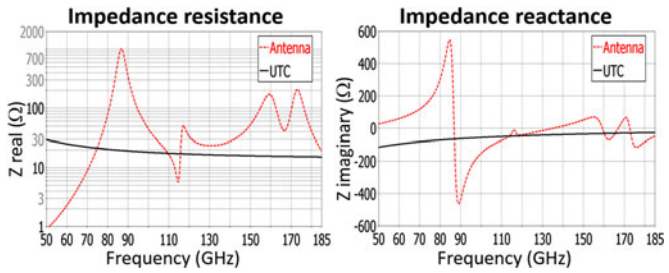

Fig. 6. Comparison between real and imaginary parts of the bow-tie antenna impedance and those measured and calculated for a 3 × 15 μm^2 area UTC at −2 V bias in [30].

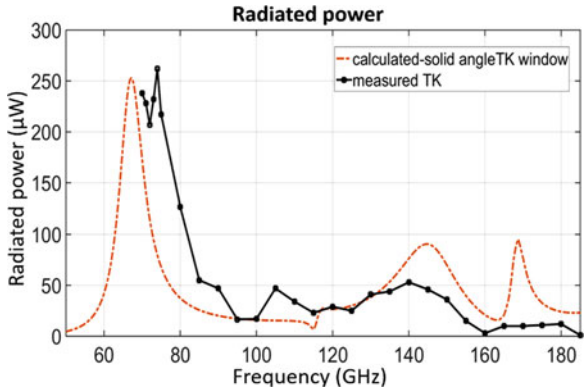

Fig. 7. The dash-dot curve is the absolute radiated power calculated with 3D full-wave modelling. The continuous black curve represents the absolute radiated power measured with a Thomas Keating (TK) power meter; the measurements were not performed above 185 GHz as the detected signal reached the minimum level detectable by the TK power meter.

full-wave modelling and using the knowledge of the UTC output impedance to take the UTC-to-antenna coupling efficiency into account. The antenna chip had an unintended gold screen deposited underneath the InP substrate. The gold screen was not to operate as a ground plane for the antenna emission, therefore the whole antenna chip did not represent an optimum design for radiation with a ground plane and no special performance was expected from its operation. To reiterate the importance of full-wave modelling, it is noted that this antenna chip configuration could not be studied by simple analytical methods. Even the horizontal substrate size strongly affects the operation and simplifying the analysis by assuming the horizontal chip size as infinite would change the performance dramatically. The calculated real and imaginary parts of the antenna impedance are plotted in Fig. 6 and compared with those measured and modelled in [33] for the UTC.

A direct comparison between calculated and measured radiated power is shown in Fig. 7 in μW on a linear scale. The trends of measured and calculated power over the frequency range are clearly correlated and show good agreement. The peaks of measured power at 74 GHz and 140 GHz correspond to the peaks of calculated power at 67 GHz and 145 GHz; it is apparent that at these frequencies complex-conjugate matching is approached.

The small peak of measured power at 105 GHz seems to correspond to the feature in the calculated power around 115 GHz; we found that both position and prominence of this calculated feature are quite sensitive to the chip width and length which were not known precisely as the chip was not fabricated at UCL. The measured peak at 74 GHz and the calculated peak at 67 GHz have very similar magnitude, i.e. 262 μW (−5.8 dBm) vs 253 μW (−5.9 dBm). The measured peak at 140 GHz and the calculated peak at 145 GHz have magnitude of 53 μW (−12.7 dBm) and 90 μW (−10.4 dBm), i.e. differ by 2.3 dB. The sharp peak calculated at 168 GHz was barely detected in the measurements, which were not performed above 185 GHz as the detected signal reached the minimum level detectable by the Thomas Keating (TK) power meter, whose electrical noise-equivalent power (NEP) equals 5 μW/Hz½. It is worth noting that the calculated peak at 168 GHz is related to a fast local variation in the antenna impedance, as can be seen in Fig. 6. At this frequency the antenna impedance real part exhibits a narrow and pronounced dip, which makes it closer to the UTC impedance real part. In addition the antenna reactance exhibits a rapid increase, becoming slightly inductive as opposed to the UTC reactance which is slightly capacitive; this allows the complex-conjugate matching condition to be approached. Additionally, both the amplitude and position of the calculated peak at 168 GHz were observed to be noticeably sensitive to the chip width and length. It is the authors' opinion that this pronounced local variation of the antenna impedance at 168 GHz, responsible for the peak of calculated emitted power, is due to a fortunate combination of effects related to the exact geometrical details of the model and is barely perceivable in the real antenna chip, as is the maximum of measured power around 168 GHz. As a final remark, it is noted that a slower than estimated transit time limited response, for the UTC integrated with the bow-tie antenna, could account for the measured emitted power being more damped at higher frequencies.

The main peaks of radiated power (measured at 74 GHz and 140 GHz and calculated at 67 GHz and 145 GHz) are clearly located at frequencies where the complex-conjugate matching is approached. No maximum of radiated power is present at frequency where the antenna operates as a resonant antenna, e.g. its reactance is zero.

Following these considerations and bearing in mind the level of difficulty involved in predicting the accurate trend over the frequency range of the absolute power radiated by a system involving so many variables, the agreement between experimental and numerical results shown in Fig. 7 is very satisfactory. An accurate analysis of the absolute power emitted from an antenna integrated photodetector had not been demonstrated before. It is noted that, when the UTC-to-antenna coupling efficiency was modelled using the classical junction-capacitance/series-resistance concept, calculated and measured radiated power were in substantial disagreement.

The literature of RF and microwave antenna engineering has shown how fundamental the source- to-antenna impedance match is, to maximise the power radiated by antennas. In the more recent context of photonic THz emitters based on antenna integrated photodiodes, this aspect has so far received little attention. An emitter made up of a highly directive and efficient antenna integrated with a high power photodiode, could still be unable to radiated high levels of power if the impedance match

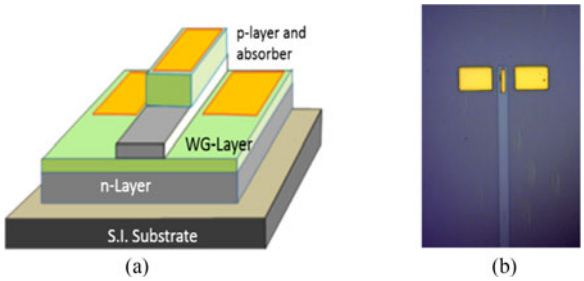

Fig. 8. (a) UTC structure with p metal contact on p-layer and absorber Ridge with integrated shallow waveguide structure with n contacts. (b) Fabricated 4 × 15 UTC prior to isolation and coupling to antenna.

between source and antenna is ignored, as most of the power generated by the photodiode could be simply rejected by the antenna. In order to optimise the photodiode-to-antenna coupling efficiency, knowledge of the source (PD) impedance is necessary; with no knowledge of the source impedance the absolute power radiated by an antenna cannot be calculated.

The capability of calculating the absolute emitted power correctly raises the possibility to further increase the power radiated by antenna integrated photodiodes via optimisation of UTC-to-antenna impedance match.

III. UTC Device Fabrication

The devices presented in this work are fabricated from three different epitaxy campaigns using similar layer structures but different growth processes (MOVPE, Solid Source MBE, Gas source MBE) [17], [18], [44]. Their epitaxial structure is shown in Table I. As can be seen the layer thicknesses are similar with the exception of the device developed for integration which includes a ridge layer to be integrated with a laser. All the devices include a waveguide layer part of the n-contact layer, to enable edge coupling of the optical input. The losses in that layer were normal for such quaternary compositions [44]. Further, the structure described in [17] incorporates a diluted waveguide design for mode conversion from an optical fibre.

The processing of antenna coupled integrated optical waveguide UTC-PDs requires several fabrication steps (Fig. 8(a)). To adhere as closely as possible to the expected device impedance and its designed matching to the antenna element, care is required to ensure that parasitic capacitance (C_p), leakage current and series resistance (R_s) are kept within the design tolerances. The fine device features required are achieved by the dry etch processing of p-ridge and optical waveguide and mesa structure by Reactive Ion Etching (RIE).

To ensure acceptable values of R_s of devices with cross-section as small as 3 μm × 10 μm, the p-contact resistivity ρ_c(p) must be in the order of 10^{-6} ohm cm^2 or less. To achieve this, Ti-Pt-Au contacts are sputtered upon the p-layer of the epitaxial layer with stringent oxide removal processing required for low contact resistance (Fig. 8(b)).

To create the p-layer (p++Q 1.3 InGaAsP) and absorber (p-InGaAs) feature, RIE was performed to etch the ridge structure. Low leakage current is ensured by the application of reagent treatments for removal of sidewall contamination and oxide growth. RIE is repeated for shallow optical waveguide etching of the InP collector layer. Ti-Pt-Au contacts are then deposited upon the waveguide layer followed by rapid thermal annealing for low resistance ohmic contacts for completion of the UTC-PD.

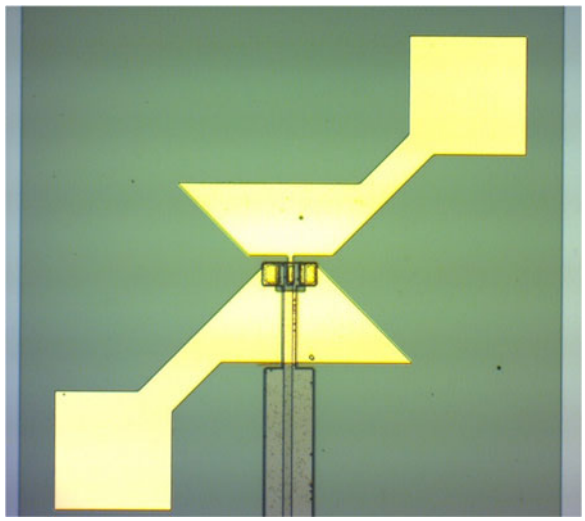

Fig. 9. Completed Antenna Coupled UTC for transmission at 250 GHz with 4 μm × 15 μm UTC_PD.

However, for the coupling of the comparatively large antenna structure to the UTC, further processing steps are performed to remove sources of parasitic capacitance and to insulate the ridge structure from the metal pathways of the antenna. This involves the etching of a mesa structure as close as practicable to the device UTC footprint down to the semi-insulating InP substrate. For the insulation of the electrical pathways to the antenna structure, a thermally rugged insulating film of suitable permittivity is deposited upon the UTC. The insulation layer will induce some parasitic capacitance due to its higher permittivity compared to an air bridge but with track features as small as 3 um mechanical support is required. To reduce the parasitic effect of the large metallic antenna structure between the device features, the mesa structure area beneath the antenna has been designed to have the least effect while maintaining the device performance. Using RIE, via holes with dimensions as small as 2 μm were etched down to the p and n contacts. Antenna structures can then be deposited upon the insulation layer for coupling to the UTC.

Finally the antenna coupled waveguide integrated UTCs (Fig. 9) are cleaved to produce facets orthogonal to the waveguide structure. A typical UTC fabricated by this method have exhibited leakage current of less than $I_{dark} = 1\ \mu$A at -1 V reverse bias. Responsivity up to 0.2 A/W for a 4 × 15 μm device without anti-reflection coating was measured using lens ended single mode fibre of 2.5 um spot size.

IV. UTC Emitter Performance

Fabricated devices can be tested using optical heterodyne measurements. THz power is measured using two versions of photoacoustic power meters; either a Thomas Keating power

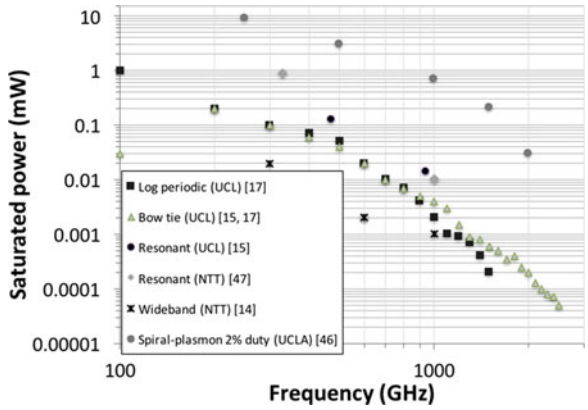

Fig. 10. Emitted power from Photomixers, including UTC PDs from this work and works from [14], [15], [17], [46], [47].

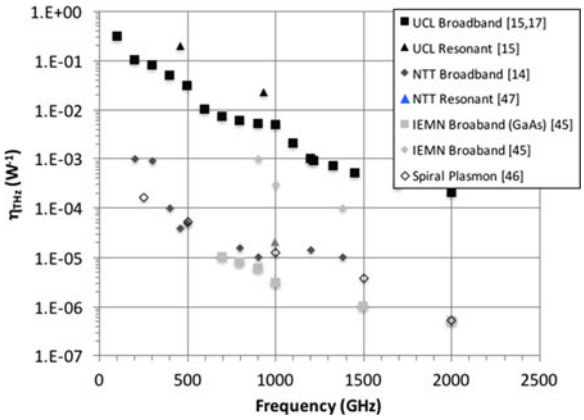

Fig. 11. Figure of Merit from set of photomixers including UTC-PDs from this work and results from [14], [15], [17], [45]–[47].

meter for high power or a Golay Cell for powers below 10 μW. The measurements were made at a given bias voltage, although changing the bias with increasing frequency would help in optimizing the output power. In that regard, the bias was optimized for frequencies of the order or 100 GHz and as such the best possible output power at THz frequencies is not represented in these results. The devices were mounted on a high resistivity silicon lens and were not actively cooled, thus also limiting the amount of power that could be achieved before the thermal destruction of the device.

Different types of integrated antennas were tested; resonant, bow tie and log periodic. Only the resonant designs made use of the modelling tools discussed in part II. All broadband designs were planned for frequencies ranging from 100 GHz to several THz.

THz emission was measured for an optical input power of 40 mW and DC photocurrent of 16 mA at frequencies up to 2.5 THz. The results are summarized in Fig. 10 and compared to a selection of the best results from UTC PDs integrated with antenna and photomixers from other groups [3], [45]–[47]. As can be seen from the broadband emitter we obtain powers ranging to 1mW at 100 GHz down to tens of nanowatts at 2.5 THz. As expected, there is a clear gain in using a resonant matched system as seen by the gain in power shown from our resonant structures and the NTT resonant devices [47]. Although these powers are not the highest obtained from photomixers [46] the highest power presented in that publication were measured under pulsed conditions, with 150 mW optical power and 2% duty cycle to avoid thermal damage. The relation with duty cycle and output power as shown in [46] works as a square of the duty cycle thus the expected THz power at 100% duty cycle would be 34 dB less than the results shown in Fig. 10. Considering this, it is more interesting to look at how efficient the devices are in converting optical to THz power. This can be done by analyzing their figure of merit that we can define as the THz power divided by the optical power squared (P_{THz}/P_{opt}^2). This metric offers the best insight into how efficiently the device convert the light into THz power and take account of the coupling of light into the device, its quantum efficiency and frequency response. We present the different published results and our device figures of merit in Fig. 11. In that case it becomes clear that the enhanced device developed in the work offer the best combination of parameters to efficiently convert light into THz power. Note that the figure of merit for the work presented in [46] was calculated by extrapolating the expected THz power for a 100% duty cycle. The devices at the lower efficiency are all vertically illuminated demonstrating the clear advantage in using waveguide design to optimize the coupling of light with the absorber of the photodetector.

The advantage in using conjugate matched antenna design can be seen. This clearly shows how key the optimization of each elements of the device design is. In particular, as discussed in Section II the coupling to the antenna and the antenna design could yield large improvement in how efficiently the devices would operate in the THz range.

V. UTC as Receivers

As receivers UTC photodiodes offer similar benefits as emitters in their tuneability and potential for integration. UTC photodiodes act as optically pumped mixers that do not require an external electrical Local Oscillator (LO) as this is generated internally via optical heterodyne generation. This allows for a wide tuning range to be achieved limited in bandwidth by the tuneability of the laser source and the response time of the photodiode.

The UTC photodiode can act as a mixer through operation under saturated conditions with strong optical pumping, on the order of 14–16 dBm. Often this requires the use of optical amplification which introduces Amplified Spontaneous Emission (ASE) noise to the photonic LO signal. This is then converted in the photodiode and contributes to the noise floor of the optoelectronic mixer and can be mitigated at the expense of tuneability by using ASE filtering, or improving fibre to chip coupling resulting in higher responsivity and removing the need for amplification.

Studies of the performance of UTC photodiodes as receivers show that the main limitations are the large conversion losses encountered ranging from 20 dB to 60 dB, depending on the device design and epitaxy [17], [18], [44]. Despite this however high detector sensitivity levels around -120 dBm/Hz at optimum operating conditions without the use of optical amplification are predicted [48].

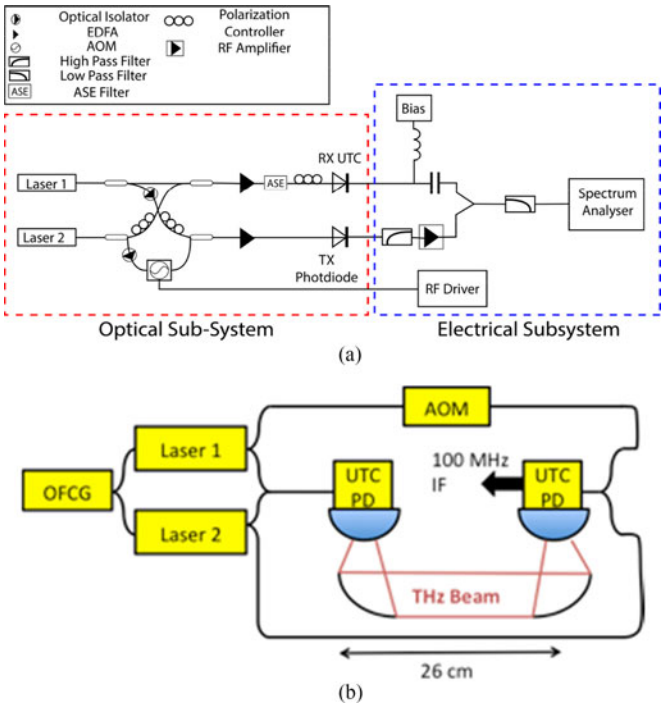

Fig. 12. 2 Experimental system diagram for mixing (a) lower frequency mixing mechanism analysis. (b) Full bandwidth mixing experiment on antenna integrate devices. The IF was measured using a spectrum analyser.

The first step in using these devices as receivers is to analyse the optimum point of operation and the mechanism for mixing. This work was done using the devices described in [44]. For this study the performance of the UTC was carried out using a self-heterodyne arrangement where the optical heterodyne for both the RF and LO signals are provided from the same pair of lasers with the LO laser 2 tone being shifted by an offset frequency provided by an Acousto-Optic Modulator (Fig. 12(a)). The optical heterodyne generated RF is mixed with the optical heterodyne generated LO inside the receiver UTC photodiode, and the IF extracted, typically through the DC bias lines via an external bias tee.

The performance of the UTC photodiode as an optoelectronic mixer is dependent on several operating parameters of the device; the optical pump power, the reverse bias voltage, and the incoming RF power. The dependence of the conversion loss on pump power and bias voltage with a constant RF power is shown in Fig. 13.

As the optical pump power is increased the optimum reverse bias point increases, in this case, this is due to an increasing space charge accumulation in the depletion layer of the device. This is demonstrated through looking at the compression of the LO signal at a fixed optical heterodyne spacing and increasing the optical power.

Fig. 14 shows around 8 dBm of optical pump power is the point at which saturation occurs at 0 V bias for this device. This point is shifted as the bias voltage is increased. In other UTC photodiode designs the space charge effect is also observed, due to undoped absorber sections of the devices. These regions show an increase in capacitance as saturation occurs [49], associated

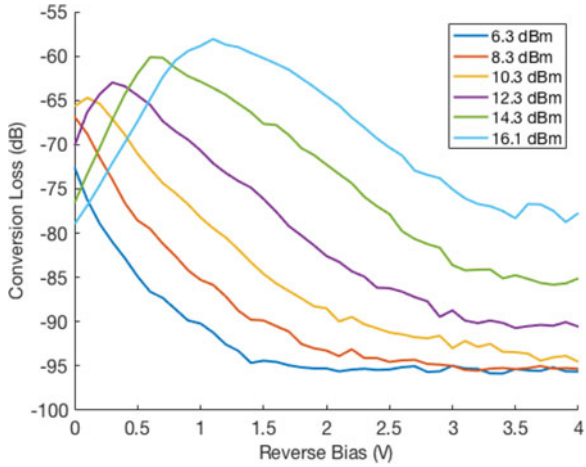

Fig. 13. Conversion Loss dependence on optical pump power and reverse bias voltage for input RF 53.04 GHz and LO 53 GHz.

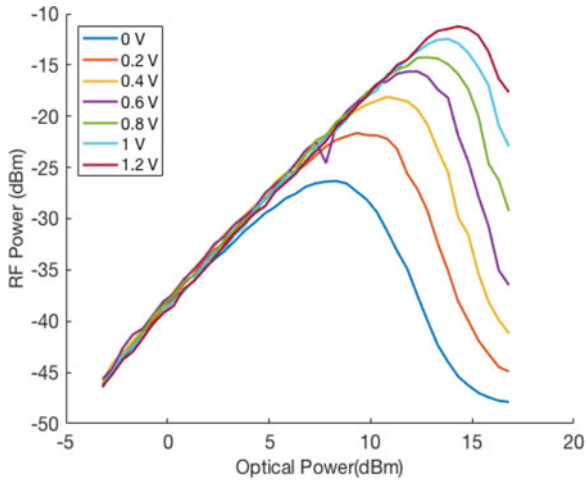

Fig. 14. Optical Heterodyne LO Signal at 53 GHz increasing the optical pump power for increasing reverse bias voltages with no applied RF input.

with an accumulation of carriers in this region. As the input optical pump signal is modulated by the optical heterodyne, the resulting capacitance is time varying at the frequency of the optical heterodyne. This nonlinear element is proposed as the mechanism for observed harmonics in p-i-n photodiodes in [50] and was proposed to also be the main mixing mechanism in UTC-PDs [49], [51].

Under optimum operating conditions the lowest conversion loss observed was 60 dB in this particular device (Using gas source MBE growth-Table I). The SNR measured was 35 dB (Fig. 15) where the main source of noise was signal spontaneous associated with the amplified photonic pump signal.

To further the study of the devices integrated with antenna the setup was extended (Fig. 12(b)) enabling measurement across the THz range. In that setup the devices were mounted on high resistivity silicon lenses. The beam was collimated through parabolic mirror and the distance between each devices was 26 cm. The IF was measured with an electrical spectrum analyzer. Note that the distance from the lenses to the mirror and the angle of the mirrors were used to fully optimize coupling

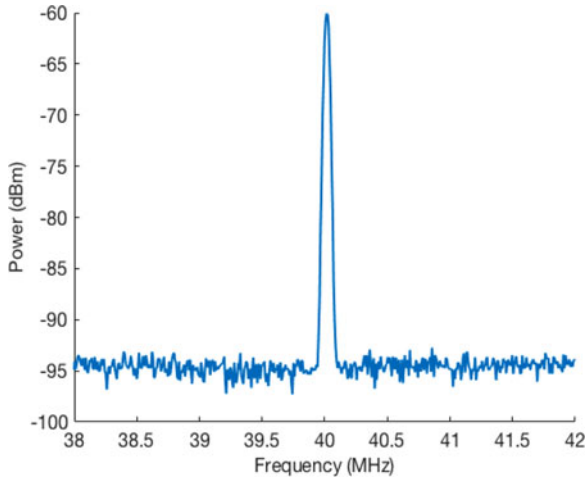

Fig. 15. Electrical spectrum of optoelectronic mixing IF signal (20 kHz resolution bandwidth).

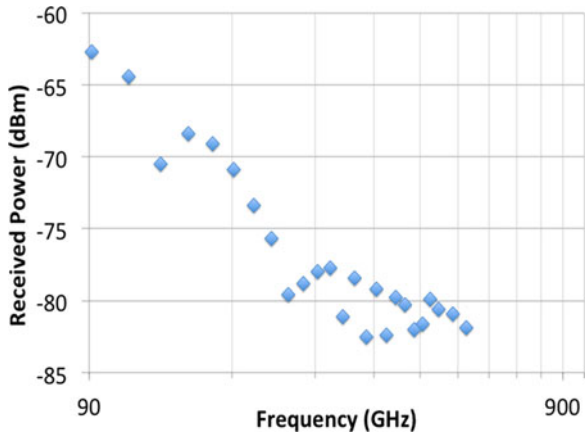

Fig. 16. Received IF power at 100 MHz as a function of the THz transmitted frequency.

between the devices. This was done at each frequency point has the beam shape changes with frequency.The device used in this measurement was slightly different [17] (TW-UCT-PD in Table I) and did offer lower conversion losses of −30 dB [52]. The device chosen was integrated with a bow-tie antenna. The emitter side was driven with a 2 mA photocurrent and 10 mW optical power while the receiver side was working at 16 mA photocurrent and 80 mW optical power provided from an erbium doped fibre amplifier. The measurement was possible up to 564 GHz where we reached the noise floor of the system (Fig. 16). Interestingly the conversion loss remained stable at around 30 dB across the frequency range (Fig. 17) and similar performance is expected at higher frequencies.

As discussed in [48], the main limitation in terms of detector sensitivity is the noise contribution by the optical amplification used to achieve saturation. Potential mitigations to this would be reducing the overall footprint of the device; the results discussed in this paper utilize a 3×15 μm^2 UTC photodiode. Lower saturation powers observed for smaller area photodiodes, coupled with an increase in responsivity through improved fibre to chip coupling such as an integrated mode converter waveguide, would also reduce the need for optical amplification. In this case, the main noise limitation would be shot noise [48].

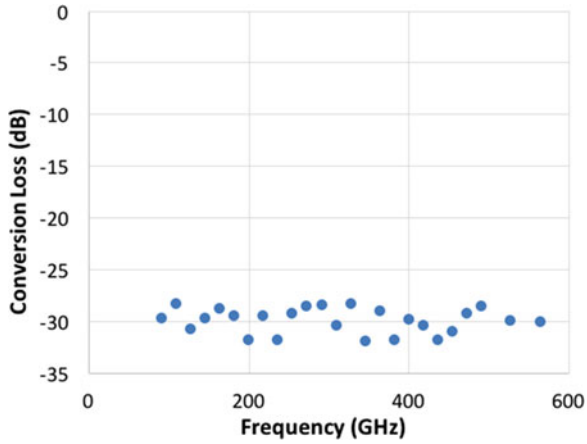

Fig. 17. Conversion loss on the UTC-PD optoelectronically pumped mixer across the detected frequency range.

VI. Conclusion

We have defined the design parameters to optimise waveguide coupled UTC-PDs integrated with planar antennas. In particular, we outline the importance of determining the impedance of the UTC-PD across the frequency range. Device performance was measured and showed high saturation power across the frequency range up to 2.5 THz, comparable with other similar sources. As expected from the design, the resonant antenna integrated devices offered better performance. Further to the outstanding emitter performance, it was demonstrated that the waveguide integrated devices were the most efficient photomixers currently developed in the THz range. We also demonstrated the use of the antenna integrated UTC-PDs as receivers. In that case one could observe that optimum mixing occurs at saturation indicating that time varying capacitance and modulated carrier velocity are the likely cause of mixing [50], [51]. This was used to demonstrate for the first time their capacity to be used as detectors for frequencies up to 560 GHz. Although the efficiency of the device is the highest reported to date, there are still possible improvements to be achieved with further design of the optical coupling element with the possible integration with plasmonic techniques which have shown interesting improvements in device performance [46]. Future work will include further optimisation of the integrated antennas using the design methodology described in this paper.

References

[1] D. Trommer *et al.*, "Ultrafast, high-power waveguide fed photodetector with integrated spot size converter," in *Proc. 2000 Int. Conf. Indium Phosphide Related Mater.*, Williamburg, VA, USA, pp. 462–465, 2000.

[2] G. Zhou *et al.*, "High-power InP-based waveguide integrated modified uni-traveling-carrier photodiodes," *J. Lightw. Technol.*, vol. 35, no. 4, pp. 717–721, Feb. 2017.

[3] H. Ito, T. Furuta, F. Nakajima, K. Yoshino, and T. Ishibashi, "Photonic generation of continuous THz wave using uni-traveling-carrier photodiode," *IEEE J. Lightw. Technol.*, vol. 23, no. 12, pp. 4016–4021, Dec. 2005b.

[4] A. J. Seeds *et al.*, "Coherent terahertz photonics," *Opt. Express*, vol. 21, no. 19, pp. 22988–23000, Sep. 2013.

[5] H. Eisele, "State of the art and future of electronic sources at terahertz frequencies," *Electron. Lett.*, vol. 46, no. 26, pp. s8–s11, 2010.

[6] C. Mann, "Practical challenges for the commercialisation of terahertz electronics," in *Proc. Int. Symp. IEEE MTT-S Microw.*, Jun. 2007, pp. 1705–1708.

[7] T. Ishibashi, S. Kodama, N. Shimizu, and T. Furuta, "High-speed response of uni-traveling-carrier photodiodes," *Jpn. J. Appl. Phys.*, vol. 36, no. 10, pp. 6263–6268, 1997.

[8] H. Ito *et al.*, "High-speed and high-output InP-InGaAs unitraveling-carrier photodiodes," *IEEE J. Sel. Topics Quantum Electron.*, vol. 10, no. 4, pp. 709–727, Apr. 2004.

[9] T. Ishibashi, Y. Muramoto, T. Yoshimatsu, and H. Ito, "Unitraveling-carrier photodiodes for terahertz applications," *IEEE J. Sel. Topics Quantum Electron.*, vol. 20, no. 6, pp. 79–88, Nov./Dec. 2014.

[10] A. Beling, Z. Li, Y. Fu, H. Pan, and J. C. Campbell, "High-power and high-linearity photodiodes," in *Proc. 24th Annu. Meet. IEEE Photon. Soc.*, Oct. 2011, vol. 1, pp. 19–20.

[11] H. Ito, T. Furuta, S. Kodama, and T. Ishibashi, "InP/InGaAs uni-travelling-carrier photodiode with 310 GHz bandwidth," *Electron. Lett.*, vol. 36, no. 21, pp. 1809–1810, 2000.

[12] C. C. Renaud, D. Moodie, M. Robertson, and A. J. Seeds, "High output power at 110 GHz with a waveguide uni-travelling carrier photodiode," in *Proc. 20th Annu. Meet. IEEELasers Electro-Opt. Soc.*, 2007, pp. 782–783.

[13] H. Ito *et al.*, "High-power photonic millimetre wave generation at 100 GHz using matching-circuit-integrated uni-travelling-carrier photodiodes," *IEE Proc. Optoelectron.*, vol. 150, no. 2, pp. 138–142, 2003.

[14] H. Ito, F. Nakajima, T. Furuta, and T. Ishibashi, "Continuous THz-wave generation using antenna-integrated uni-travelling-carrier photodiodes," *Semicond. Sci. Technol.*, vol. 20, no. 7, pp. S191–S198, Jul. 2005.

[15] C. Renaud *et al.*, "A high responsivity, broadband waveguide uni-travelling carrier photodiode," *Proc. SPIE*, vol. 6194, no. 1, pp. C1940–C1940, 2006.

[16] H. J. Song *et al.*, "Uni-travelling-carrier photodiode module generating 300 GHz power greater than 1 mW," *IEEE Microw. Wireless Compon. Lett.*, vol. 22, no. 7, pp. 363–365, Jul. 2012.

[17] E. Rouvalis, C. C. Renaud, D. G. Moodie, M. J. Robertson, and A. J. Seeds, "Continuous wave terahertz generation from ultra-fast InP-based photodiodes," *IEEE Trans. Microw. Theory Tech.*, vol. 60, no. 3, pp. 509–517, Mar. 2012.

[18] M. Natrella *et al.*, "InGaAsP-based uni-travelling carrier photodiode structure grown by solid source molecular beam epitaxy," *Opt. Express*, vol. 20, no. 17. pp. 19279–19288, 2012.

[19] H. Ito and T. Ishibashi, "Terahertz-wave generation using resonant-antenna-integrated uni-traveling-carrier photodiodes," *Proc. SPIE*, vol. 10209, 2017, Art. no. 102090R.

[20] R. S. Tahim, G. M. Hayashibara, and K. Chang, "Design and performance of W-band broad-band integrated circuit mixers," *IEEE Trans. Microw. Theory Tech.*, vol. 31, no. 3, pp. 277–283, Mar. 1983.

[21] G. A. Ediss, S. J. Wang, and N. J. Keen, "Quasioptical components for 230 GHz and 460 GHz," *IEE Proc. H Microw., Antennas Propag.*, vol. 132, no. 2, pp. 99–106, Apr. 1985.

[22] G. A. Ediss, "Technical memorandum. Dual-mode horns at millimetre and submillimetre wavelengths," *IEE Proc. H Microw., Antennas Propag.*, vol. 132, no. 3, pp. 215–218, 1985.

[23] H. R. Fetterman *et al.*, "Far-ir heterodyne radiometric measurements with quasioptical Schottky diode mixers," *Appl. Phys. Lett.*, vol. 33, no. 2, pp. 151–154, 1978.

[24] E. Sauter, G. V. Schultz, and R. Wohlleben, "Antenna patterns of an open structure mixer at a submillimeter wavelength and of its scaled model," *Int. J. Infrared Millim. Waves*, vol. 5, no. 4, pp. 451–463, 1984.

[25] E. N. Grossman, "The coupling of submillimeter corner-cube antennas to Gaussian beams," *Infrared Phys*., vol. 29, no. 5, pp. 875–885, 1989.

[26] J. Zmuidzinas, A. L. Betz, and R. T. Boreiko, "A corner-reflector mixer mount for far infrared wavelengths," *Infrared Phys*., vol. 29, no. 1, pp. 119–131, 1989.

[27] S. S. Gearhart, C. C. Ling, and G. M. Rebeiz, "Integrated millimeter-wave corner-cube antennas," *IEEE Trans. Antennas Propag.*, vol. 39, no. 7, pp. 1000–1006, Jul. 1991.

[28] S. S. Gearhart, C. C. Ling, G. M. Rebeiz, H. Davee, and G. Chin, "Integrated 119-μm linear corner-cube array," *IEEE Microw. Guided Wave Lett.*, vol. 1, no. 7, pp. 155–157, Aug. 1991.

[29] G. M. Rebeiz, "Millimeter-wave and terahertz integrated circuit antennas," *Proc. IEEE*, vol. 80, no. 11, pp. 1748–1770, 1992.

[30] J. D. Kraus, R. J. Marhefka, and A. S. Khan, *Antennas For All Applications*, 3rd ed. Boston, MA, USA: McGraw-Hill, 2010.

[31] D. P. Neikirk *et al.*, "Far-infrared imaging antenna arrays," *Appl. Phys. Lett.*, vol. 40, no. 3, pp. 203–205, 1982.

[32] A. V. Boriskin *et al.*, "Lens or resonator? Electromagnetic behavior of an extended hemielliptic lens for a sub-millimeter-wave receiver," *Microw. Opt. Technol. Lett.*, vol. 43, no. 6, pp. 515–518, Dec. 2004.

[33] M. Natrella *et al.*, "Accurate equivalent circuit model for millimetre-wave UTC photodiodes," *Opt. Express*, vol. 24, no. 5, pp. 4698–4713, 2016.

[34] J. Dyson, "The equiangular spiral antenna," *IRE Trans. Antennas Propag.*, vol. 7, no. 2, pp. 181–187, 1959.

[35] R. DuHamel and D. Isbell, "Broadband logarithmically periodic antenna structures," *IRE Int. Conv. Rec.*, vol. 5, pp. 119–128, 1957.

[36] M. Natrella *et al.*, "Modelling and measurement of the absolute level of power radiated by antenna integrated THz UTC photodiodes," *Opt. Express*, vol. 24, no. 11, 2016, Art. no. 11793.

[37] G. Lucovsky, M. E. Lasser, and R. B. Emmons, "Coherent light detection in solid-state photodiodes," *Proc. IEEE*, vol. 51, no. 1, pp. 166–172, 1963.

[38] M. N. Hutchinson, F. Bucholtz, C. R. S. Williams, and J. M. Nichols, "Estimating the complex impedance of an MUTC photodetector," *J. Lightw. Technol.*, vol. 35, no. 12, pp. 2444–2450, Jun. 2017.

[39] H. Kroemer, "Heterostructure bipolar transistors and integrated circuits," *Proc. IEEE*, vol. 70, no. 1, pp. 13–25, 1982.

[40] H. Kroemer, "Heterostructure bipolar transistors: What should we build?," *J. Vacuum Sci. Technol. B*, vol. 1, no. 2, pp. 126–130, 1983.

[41] R. L. Anderson, "Experiments on Ge-GaAs heterojunctions," *Solid State Electron.*, vol. 5, no. 5, pp. 341–351, 1962.

[42] A. A. Grinberg, M. S. Shur, R. J. Fischer, and H. Morkoc, "An investigation of the effect of graded layers and tunneling on the performance of AlGaAs/GaAs heterojunction bipolar transistors," *IEEE Trans. Electron Devices*, vol. 31, no. 12, pp. 1758–1765, Dec. 1984.

[43] V. Ryzhii and M. Shur, "Tunnelling- and barrier-injection transit-time mechanisms of terahertz plasma instability in high-electron mobility transistors," *Semicond. Sci. Technol.*, vol. 17, no. 11, pp. 1168–1171, 2002.

[44] E. Rouvalis *et al.*, "High-speed photodiodes for InP-based photonic integrated circuits," *Opt. Express*, vol. 20, pp. 9172–9177, 2012.

[45] E. Peytavit *et al.*, "Milliwatt-level output power in the sub-terahertz range generated by photomixing in a GaAs photoconductor," *Appl. Phys. Lett.*, vol. 99, no. 22, 2011, Art. no. 223508..

[46] C. W. Berry *et al.*, "High power terahertz generation using 1550 nm plasmonic photomixers," *Appl. Phys. Lett.*, vol. 105, 2014, Art. no. 011121.

[47] F. Nakajima, T. Furuta, and H. Ito, "High-power continuous-terahertz-wave generation using a resonant-antenna-integrated uni-traveling-carrier photodiode," *Electron. Lett.*, vol. 40, pp. 1297–1299, 2004.

[48] C. C. Renaud *et al.*, "Uni-Travelling carrier photodetectors as THz detectors and emitters," *Proc. SPIE*, vol. 9370, 2015, Art. no. 93700B.

[49] H. Fushimi, T. Furuta, T. Ishibashi, and H. Ito, "Photoresponse nonlinearity of a uni-traveling-carrier photodiode and its application to optoelectronic millimeter-wave mixing in 60 GHz band," *Jpn. J. Appl. Phys.*, vol. 43, pp. L966–L968, 2004.

[50] K. J. Williams, R. D. Esman, and M. Dagenais, "Nonlinearities in p-i-n microwave photodetectors," *J. Lightw. Technol.*, vol. 14, no. 1, pp. 84–96, Jan. 1996.

[51] T. Nagatsuma *et al.*, "Continuous-wave terahertz spectroscopy system based on photodiodes," *PIERS Online*, vol. 6, pp. 390–394, 2010.

[52] E. Rouvalis, M. J. Fice, C. C. Renaud, and A. J. Seeds, "Millimeter-wave optoelectronic mixers based on uni-traveling carrier photodiodes," *IEEE Trans. Microw. Theory Tech.*, vol. 60, no. 3, pp. 686–691, Mar. 2012.

Cyril C. Renaud (M'08–SM'12) received the Engineering degree from the Ecole Supérieure d'Optique, Orsay, France, and the Diplôme d'Etudes Approfondies (D.E.A.) in optics and photonics from the University Paris XI, Orsay, in 1996. He received the Ph.D. degree in 2001. He spent one year as a Project Engineer with Sfim-ODS, working on the development of microchips lasers and portable range finders. He, then, joined the Optoelectronics Research Centre, University of Southampton, Southampton, U.K., in 1998, to work on diode pumped high-power ytterbium-doped fiber-lasers, with particular interest on Q-switched system and 980-nm generation. He is currently a Reader in photonics at the University College London (UCL), London, U.K., and the UCL Site Director for the UCL/Cambridge Doctoral Training Centre in Integrated Photonic and Electronic Systems. His has published more than 140 peer reviewed journals and international conferences, and three patents.

Michele Natrella received the five-year Laurea degree in electronic engineering from Politecnico di Bari, Bari, Italy, in 2006. He received the Ph.D. degree in photonics in 2015. He spent a year in industry working as a Design Engineer within the electronic security systems sector. He was, then, employed as a Research Engineer at the Applied Research Organisation CETMA, Brindisi, Italy. Here he spent three years, conducting research on wireless communications, laser range finders, and software development. He moved to academia in October 2010, when he joined the Ultrafast Photonics Group, University College London (UCL), U.K., employed as a Marie Curie Researcher, to work on the development of photonic terahertz emitters and receivers. He is currently a Senior Research Associate in the Department of Electronic and Electrical Engineering, UCL. His research in Academia has led to 21 publications in peer reviewed journals and international conferences.

Chris Graham received the B.Eng. degree from the University of Essex, Colchester, U. K. He Joined Ultrafast Photonics Group, Department of Electronic and Electrical Engineering, University College London, London, U.K., in 2006. He received Ph.D. degree in ultrafast photonic switches for sampling applications in 2011. He has worked as a Research Associate in the Photonics Group for the last 7 years working in the fields of uni-travelling photodiode design fabrication and evaluation; photonic integrated circuit packaging and ultrafast photoconductors. His published more than 20 peer reviewed journals and international conferences, and 1 patent.

James Seddon received the B.Sc. degree in chemistry from the University of Plymouth, Plymouth, U.K., the M.Sc. degree in nanoscience and technology from the University of Sheffield, Sheffield, U.K., and the M.Res. degree in integrated photonic and electronic systems from the University College London, London, U.K. He is currently working toward the Ph.D. with the Ultrafast Photonics Group, University College London, working on the development of a terahertz lab-on-chip spectroscopy platform.

Frederic Van Dijk was born in Chevreuse, France, in 1972. He received the Ph.D. degree from Université Paul Sabatier, Toulouse, France, in 1999. His performed at the Laboratory for Analysis and Architecture of Systems, Centre National de la Recherche Scientifique, Toulouse, dealt with growth, process, and characterization of AlGaAs/GaAs vertical cavity surface emitting laser structures.

In 2000, he joined Thales Research and Technology, Orsay, France. He is currently with III-V Lab, Palaiseau, France, where he is involved in design, fabrication, and characterization of laser sources for microwave applications. His current research interests include directly modulated distributed feedback lasers, mode-locked lasers for frequency synthesis and clock recovery, and microwave photonics.

Alwyn J. Seeds received the B.Sc., Ph.D., and D.Sc. degrees from the University of London, London, U.K. From 1980 to 1983, he was a Staff Member at Lincoln Laboratory, Massachusetts Institute of Technology, where he worked on GaAs monolithic millimetre-wave integrated circuits for use in phased-array radar. Following three years as Lecturer in telecommunications at Queen Mary College, University of London, then he moved to University College London, London, U.K., in 1986, where he is currently a Professor of Opto-electronics and the Head of the Photonics Group. He has published more than 350 papers on microwave and opto-electronic devices and their systems applications. His current research interests include photonic integration, semiconductor opto-electronic devices, and wireless and optical communication systems.

Dr. Seeds is a Fellow of the Royal Academy of Engineering, U.K. He has been a Member of the Board of Governors and Vice-President for Technical Affairs of the IEEE Photonics Society (USA). He has served on the programme committees for many international conferences. He is a cofounder of Zinwave, a manufacturer of wireless over fiber systems. He received the Gabor Medal and the Prize of the Institute of Physics in 2012.